



# Physics-informed neural networks for modeling mesoscale heat transfer using the Boltzmann transport equation

**Jiahang Zhou, Ruiyang Li, and Tengfei Luo**

Department of Aerospace and Mechanical Engineering, University of Notre Dame, Notre Dame, IN, United States

## Contents

1. Introduction	212
2. Physics-informed neural networks (PINNs) in scientific computation	214
2.1 PINN applications in the field of fluid dynamics	215
2.2 PINN applications in the field of heat transfer	216
3. PINN for solving phonon BTE	217
3.1 Solve steady-state phonon BTE under a small temperature difference	217
3.2 Solve steady-state phonon BTE under arbitrary temperature differences	226
3.3 Solve transient phonon BTE	233
4. Conclusion and perspective	235
Appendix	236
References	236

## Abstract

The phonon Boltzmann transport equation (BTE) is a vital tool for bridging the atomic scale and macroscale heat transfer because it has been proven to be capable of accurately describing phonon transport in the mesoscale. Compared to Fourier's law, phonon BTE can capture the ballistic-diffusive heat conduction when the characteristic lengths are similar to the phonon mean free path. However, numerically solving phonon BTE is extremely computationally costly due to its high dimensionality, especially when phonon dispersion and time evolution are considered. Recently, physics-informed neural networks (PINNs) have been successfully applied to approximate both stationary and transient phonon BTE solutions, exhibiting superior efficiency and accuracy. Moreover, the PINN scheme can be training data-free and learn the solutions to phonon BTE in parameterized spaces (such as geometric parameters and domain temperature differences), allowing a trained model to quickly evaluate thermal transport

of structures with different geometries and under different temperature differences. With high efficiency and accuracy, the PINN technique shows great promise for practical applications, such as thermal design and thermal management of microelectronic devices.



## 1. Introduction

Thermal management is critically important as small footprint, lightweight, low cost, high performance, and high reliability [1] are intensely pursued in electronics. As industry is deploying components with higher power consumption inside smaller packages, micro and nanoscale thermal analysis becomes necessary for designing and advancing electronic devices. Moreover, the rapid development of micro/nano technology brings the characteristic length of those devices down to the level comparable to or even smaller than the mean free path of phonons, the primary thermal energy carriers in semiconductors. Under this circumstance, phonon transport is not purely diffusive and can be ballistic. For the last two centuries, the conventional Fourier's law has been widely used for analyzing macroscale thermal behaviors. However, various striking phenomena that Fourier's law cannot explain have been discovered, such as the quantization of thermal conductance and Anderson localization [2]. Specifically, Fourier's law is not applicable for accurately demonstrating the heat transfer phenomena when the length scale is comparable to or smaller than the phonon mean free path or when the time scale is shorter than the average phonon relaxation time. The phonon Boltzmann transport equation (BTE) [3] can accurately describe phonon transport across the nanoscale to the macroscale, and it has been proven to be able to model heat conduction problems in sub-micron geometries precisely.

In order to solve the phonon BTE, isotropic wave vector space and the single-mode relaxation time (SMRT) approximation are usually adopted to simplify the computation [4]. The energy-based phonon BTE, under the SMRT approximation can be written as,

$$\frac{\partial e}{\partial t} + \boldsymbol{\nu} \cdot \nabla e = \frac{e^{eq} - e}{\tau} \quad (1)$$

where  $e(\mathbf{x}, \mathbf{s}, k, p, t) = \hbar \omega D(\omega, p)[f - f^{eq}(T_{ref})]$  is the phonon energy deviational distribution function,  $e^{eq}(k, p, T) = \hbar \omega D(\omega, p)[f^{eq}(T) - f^{eq}(T_{ref})]$  is the associated equilibrium distribution function,  $\boldsymbol{\nu}$  is the group velocity, and  $\tau$  is the effective relaxation time. Under the SMRT approximation, each

phonon mode is assigned a specific relaxation time corresponding to the net effect of various phonon scattering processes. The equilibrium phonon distribution function  $f^{eq}(\omega, T)$  follows the Bose-Einstein distribution,

$$f^{eq}(\omega, T) = \frac{1}{e^{\frac{\hbar\omega}{k_B T}} - 1} \quad (2)$$

where  $\hbar$  is Planck's constant divided by  $2\pi$ ,  $k_B$  is the Boltzmann constant,  $\omega$  is the angular frequency, and  $T$  is the temperature. The phonon distribution function  $f = f(\mathbf{x}, \mathbf{s}, k, p, t)$  (or  $f(\mathbf{x}, \mathbf{s}, \omega, p, t)$ ) is a function determined by spatial vector  $\mathbf{x}$ , directional unit vector  $\mathbf{s} = (\cos\theta, \sin\theta\cos\varphi, \sin\theta\sin\varphi)$  ( $\theta$  is the polar angle and  $\varphi$  is the azimuthal angle), time  $t$ , wave number  $k$  (or angular frequency  $\omega = \omega(k, p)$ ) and polarization  $p$ . Assuming that the temperature difference throughout the whole domain is much smaller than the reference temperature (i.e.,  $|\Delta T| \ll T_{ref}$ ), we can use the following approximation [5],

$$e^{eq}(k, p, T) = \hbar\omega D(\omega, p) [f^{eq}(\omega, T) - f^{eq}(\omega, T_{ref})] \approx C(\omega, p)(T - T_{ref}) \quad (3)$$

where  $D(\omega, p) = \frac{k^2}{2\pi^2|\mathbf{v}|}$  is the phonon density of states, and  $C(\omega, p) = \hbar\omega D(\omega, p) \frac{\partial f^{eq}}{\partial T}$  represents the modal heat capacity. The problem can be significantly simplified with this assumption, which is only applicable to cases with small temperature differences. Further, the group velocity  $\mathbf{v} = \nabla_k \omega$  and relaxation time  $\tau(\omega, p, T)$  can be obtained through the phonon dispersion relation. Due to the energy conservation of the scattering term, Eq. (4) should be satisfied,

$$\sum_p \int_0^{\omega_{max,p}} \int_{4\pi} \frac{e^{eq} - e}{\tau} d\Omega d\omega = 0 \quad (4)$$

where  $\omega_{max,p}$  is the maximum frequency. The local temperature can be obtained by substituting Eq. (3) into Eq. (4),

$$T = T_{ref} + \frac{1}{4\pi} \left( \sum_p \int_0^{\omega_{max,p}} \int_{4\pi} \frac{e}{\tau} d\Omega d\omega \right) \times \left( \sum_p \int_0^{\omega_{max,p}} \frac{C}{\tau} d\omega \right)^{-1} \quad (5)$$

Despite the superiority in precisely capturing micro-nanoscale thermal transport behavior, numerically solving phonon BTE can be much more computationally challenging than solving Fourier's law, especially when phonon dispersion and time evolution are considered. To address this issue, the discrete ordinate method (DOM) is applied to solve BTE directly using

finite element or finite difference methods, where the solid angle space is discretized to capture non-equilibrium phonon distribution. However, it usually requires large computation memory, and a high convergence rate is difficult to achieve, especially in the diffusive limit [6,7]. Recently, an implicit kinetic scheme (IKS) was developed to solve 1D and 2D phonon BTEs accurately within a few minutes [8]. But for 3D calculations, it takes more than an hour for a large-scale parallel numerical solver with 400 processors to run a single-step simulation [9]. Typically, most numerical solvers require extensive computation resources to run the simulations and may encounter problems while handling high-dimension cases.

The scope of this chapter is to introduce an alternative method to solve the phonon BTE efficiently and accurately, leveraging the new-emerging machine learning techniques to overcome the limitations of conventional numerical solvers (e.g., curse of dimensionality, difficulty in mesh generation) while learning the solutions in a parametric setting.



## **2. Physics-informed neural networks (PINNs) in scientific computation**

Deep learning takes advantage of the back-propagation algorithm to learn representations of large data sets. It has shown superior potential in discovering intricate relationships in high-dimension data sets and therefore made significant advances in solving problems in many research domains, such as computer vision [10], neuroscience [11], and natural language processing [12]. Moreover, deep learning has shown great potential in scientific computing, particularly in solving partial differential equations (PDEs). Many well-developed numerical solvers can tackle various PDEs based on finite difference (FD), finite volume (FV), finite element (FE), and other methods. However, some of their practical applications have proven to be limited due to the curse of dimensionality, which means the computational cost and the complexity of nonlinear regression models increase exponentially with the dimensionality [13]. In contrast, it has been shown that deep neural networks (DNNs) can approximate smooth functions [14] and overcome the curse of dimensionality in approximating the numerical solutions of a class of nonlinear PDEs [15]. In addition, compared to mesh-based numerical solvers, deep learning can learn the solution to the PDE by minimizing the PDE residual and taking advantage of the automatic differentiation of DNNs [16], avoiding the burden of mesh generation, especially when moving boundaries and deforming geometries are considered.

The concept of PINNs was first brought up in 2019 and leveraged to solve the fluid dynamics problems [16]. PINNs are trained with respect to any given physics laws described by PDEs, with little or even no need for labeled training data, depending on the extent of known laws of physics. This technique has been successfully applied in fluid dynamics, and more recently, heat transfer, establishing the potential for applications in even more research fields.

## 2.1 PINN applications in the field of fluid dynamics

Accurately and efficiently simulating fluid flow has been of great importance and indispensable in many research fields, e.g., aerospace engineering, biomedical engineering, meteorology, and oceanography. The fluid system is typically governed by incompressible or compressible Navier-Stokes equations, depending on whether the density of fluids changes with the flow. Navier-Stokes equations is a highly nonlinear PDE system, which can be solved numerically by discretization and iteratively solving large linear/nonlinear systems. PINN has been one of the focal points in fluids research in recent years, and a wide range of techniques have been developed to address specific problems in PINN. Knowing these activities is essential in learning how PINN can be leveraged to solve heat transfer problems. PINN has been employed for large-eddy simulations to incorporate physics insights into data-based wall modeling [17]. It is shown that the inclusion of physical laws would enhance the extrapolation capabilities of the neural network and proved the proposed method outperforms the conventional equilibrium model in a non-equilibrium flow. To study high-speed flow, both one-dimensional and two-dimensional Euler equations are solved based on the PINN framework [18], and both forward/inverse problems are investigated. Moreover, a physics-constrained deep learning approach for surrogate modeling of fluid flows is devised [19] and tested on circular pipe flow, stenotic flow, and aneurysmal flow, which are relevant to practical cardiovascular applications. It is noted that this approach achieved learning the solutions of full Navier-Stokes equations in a parametric setting without relying on any labeled training data, showing a promising application in rapid geometric optimization and uncertainty quantification. For flow visualization, a physics-informed deep-learning framework called hidden fluid mechanics (HFM) is developed to extract the velocity and pressure fields directly from the images [20]. The HFM is demonstrated for several physical and biomedical problems and shows the robustness to low resolution and substantial noise in the observation data.

## 2.2 PINN applications in the field of heat transfer

PINN has also been applied to heat transfer problems, but more precisely, thermal fluidic problems. Besides the governing equations, boundary conditions are essential to a well-defined heat transfer problem. Currently, computational fluid mechanics (CFD) is a sophisticated tool to tackle heat transfer problems with complicated boundary conditions, such as complex temperature distributions imposed on heated surfaces and mixed boundary conditions. However, in real-world heat transfer applications, it is common to encounter thermal boundaries that are not known precisely. Furthermore, the ill-posed boundary value problems are beyond the scope of the ability of the CFD method. Instead, PINN is proven to tackle this kind of problem [21]. In particular, given sparse measurement data, temperature and velocity fields are accurately recovered by PINN in forced and mixed convection problems with unknown thermal boundary conditions on the heated surfaces. It shows that PINN is bridging the gap between experimental and computational heat transfer by combining multi-fidelity measurements directly with the governing equations and encapsulating them into the DNNs. As for PINN, one of the biggest advantages over traditional machine learning schemes is that PINN does not require large experimental or simulation databases, and PINN can directly solve both forward and inverse problems simultaneously, unlike surrogate models that require multiple forward solutions. Compared to numerical solvers, PINN can handle irregular geometries without the need for mesh generation, and therefore PINN is not affected by numerical error inherent in the mesh quality [22]. PINN has also been successfully applied to recover full-field temperature history and discover unknown material and process parameters in additive manufacturing processes, given partially observed temperature data measured from an infrared camera [23]. The study also investigates the application of transfer learning and finds that training epochs could be reduced by 80% when a pre-trained model is leveraged. It shows that PINN can take advantage of past results and reutilize them to accelerate new learning processes. Moreover, PINN is claimed to be simple to implement, fast and accurate for radiative transfer problems, which are 7-dimension in the most general case [24]. The study also derives a rigorous estimate on the so-called generalization error for the output of PINNs and proves that PINN will not suffer from the curse of dimensionality.

Apart from fluid dynamics and heat transfer, PINNs have also been applied in the field of finance [25], molecular dynamics simulations [26],

fiber optics [27], etc. In this chapter, we discuss how PINNs have been developed to solve the multiscale phonon Boltzmann transport equation, which is essential for understanding the mesoscale thermal transport mechanism.



### 3. PINN for solving phonon BTE

A PINN-based phonon BTE solver has been developed and extended to analyze micro-nanoscale thermal transport problems [28,29]. In particular, 1D, 2D, and 3D heat conduction problems are solved based on the PINN framework, and the results are validated by either analytical solutions of phonon BTE (for low-dimension problems) or Fourier's law (for high-dimension problems in the diffusive limit). Crystalline silicon, the most representative semiconductor material, is chosen for study. Mode-resolved properties are considered, and the characteristic length can range from the nanoscale to the macroscale, which shows promise in device-level applications.

#### 3.1 Solve steady-state phonon BTE under a small temperature difference

To predict thermal transport behavior in the micro-nanoscale domain fast and accurately, a PINN model is developed [29] to approximate the solution of the steady-state mode-resolved phonon BTE (Eq. 6). The PINN model incorporates inherent physical laws into the model structure, enabling efficient and fast prediction of the solution to phonon BTE. Unlike numerical phonon BTE solvers that solve phonon BTE iteratively on numerous nodes or cells, the PINNs framework can learn the high-dimensional solution by minimizing phonon BTE residuals on a fair number of collocation points without any labeled training data. Specifically, the phonon BTE, boundary conditions, and initial conditions are incorporated into the neural network loss function. By minimizing the loss function, the output of neural networks can approximate the solution to the phonon BTE.

$$\boldsymbol{\nu} \cdot \nabla e = \frac{e^{eq} - e}{\tau} \quad (6)$$

As shown in Fig. 1, the input variables to the neural networks are position vector  $\mathbf{x}$  (including  $x$ ,  $y$ , and  $z$ ), solid angle  $\mathbf{s}$  (including polar angle  $\theta$  and azimuthal angle  $\phi$ ), wave number  $k$ , polarization  $p$ , and additional parameters  $\boldsymbol{\mu}$ . Here,  $\boldsymbol{\mu}$  is composed of the characteristic length of the simulation

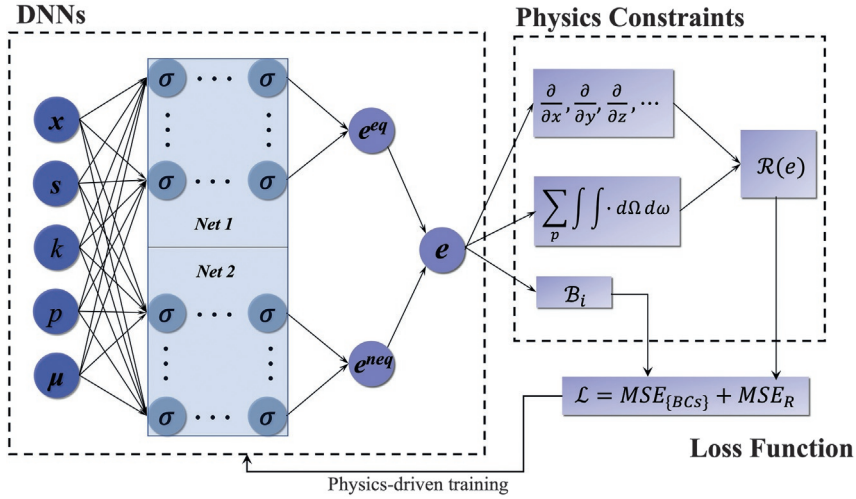


**Fig. 1** A schematic of the PINN framework for solving stationary mode-resolved phonon BTE under a small temperature difference.

domain and the phonon mean free path. Adopting characteristic lengths of the modeled structures as one of the input variables enables the PINN scheme to solve phonon BTE in a parametric setting, which is one of the key advantages over conventional numerical solvers. Conventional numerical solvers need to perform a new simulation for geometry with a different dimension, but PINN can obtain the results directly by using the desired new dimension as an input. Solving BTE numerically usually involves mesh generations and solution iterations, which can be computationally expensive, especially while tackling mode-resolved phonon BTE with a large number of variables. Moreover, solving problems with varying geometries can be even more challenging due to the need for regenerating mesh. In addition to characteristic length, phonon mean free path is also taken as one of the input variables due to its impact on phonon modes through relaxation time. Other physical variables (e.g., temperature differences, internal heat generate rates) can also be formulated into the PINN as inputs for parametric learning.

Due to the large difference between the magnitudes of equilibrium phonon energy distribution function  $e^{eq}$  and non-equilibrium phonon energy distribution function  $e^{neq}$ , especially when frequency-dependent Knudsen number  $Kn = \Lambda/L$  (the ratio of phonon mean free path and characteristic length) is extremely small (e.g.,  $Kn \sim O(10^{-4})$ ), two fully connected DNNs are adopted to approximate  $e^{eq}$  and  $e^{neq}$  separately to enhance the training



efficiency. Each sub-network shares an identical structure and maps the input variables to the target quantity of interest through several hidden layers. The output variables  $e^{eq}$  and  $e^{neq}$  are used to form phonon energy distribution function  $e$ , which is incorporated into the loss function through physical constraints, including phonon BTE, boundary conditions, and the law of energy conservation. The phonon BTE is solved by minimizing the loss function as described in Eq. (7), which is comprised of the residuals from PDE, the law of energy conservation (requires that the divergence of the heat flux must be zero for a steady-state system without internal heat source), and boundary conditions.

$$\mathcal{L} = \left\| \boldsymbol{\nu} \cdot \nabla e - \frac{e^{eq} - e}{\tau} \right\|^2 + \|\nabla \cdot \mathbf{q}\|^2 + \sum_i \|\mathcal{B}_i\|^2, \quad (7)$$

It is noted that the first derivatives of  $e$  with respect to spatial coordinates are required to calculate the residual from PDE. This can be achieved by automatic differentiation in the DNN, which uses chain rule to compute derivatives analytically and efficiently during the back-propagation process. This is a key advantage of PINN over numerical methods since evaluating the derivatives of any point in the domain no longer needs information from neighboring grid points as in numerical methods. To calculate the divergence of heat flux, one can integrate the right-hand side of Eq. (6) over the solid angle domain and frequency domain, as shown in Eq. (8),

$$\nabla \cdot \mathbf{q} = \sum_p \int_0^{\omega_{max,p}} \int_{4\pi} \frac{e^{eq} - e}{\tau} d\Omega d\omega \quad (8)$$

where the total heat flux is

$$\mathbf{q} = \sum_p \int_0^{\omega_{max,p}} \int_{4\pi} \boldsymbol{\nu} e d\Omega d\omega, \quad (9)$$

Based on the proposed PINN scheme, thermal transport problems, including 1D cross-plane, 2D in-plane, 2D square, and 3D cuboid heat conduction problems, can be evaluated at different characteristic length scales. The following sections show examples of these cases.

### 3.1.1 1D phonon transport

1D cross-plane heat conduction problem is studied based on the PINN model and validated by comparing it to the analytical solution. For low dimensional problems (i.e., 1D and 2D problems), the analytical solutions

can be obtained for simple domain geometries [30]. However, analytical solutions are impossible to obtain for high-dimension or complex-domain thermal transport problems. In the 1D heat conduction problem, silicon thin film is selected as the model structure, and the domain is governed by the 1D phonon BTE, with isothermal boundary conditions. For the silicon thin film, the dimension in the cross-plane direction is much smaller than the lateral dimensions, thus a 1D approximate is warranted. The thickness (characteristic length) of the silicon film is  $L$ , and the left boundary is maintained at high-temperature  $T_L = T_{ref} + \Delta T/2$  while the right boundary is maintained at low-temperature  $T_R = T_{ref} - \Delta T/2$ , with  $\Delta T$  set to 1 K. The setup is depicted in Fig. 2A.

In order to achieve the prediction of parametric solutions with varying domain sizes, five different characteristic lengths ranging from 10 nm to 100  $\mu\text{m}$  are selected as part of the input features. Without the need for any labeled training data, the PINN is trained by minimizing the loss function given well-organized input features. After training, the temperature and heat flux can be evaluated at new locations and unseen length scales, given the interpolation ability of DNNs.

Fig. 2B shows the predicted dimensionless temperature profile along the cross-plane direction under different length scales and the comparison with analytical solutions [30]. It is obvious that as the length scale decreases, the temperature slips phenomenon near the boundary is captured successfully, which is due to the non-diffusive phonon transport at small characteristic length scales. More importantly, PINN prediction only takes about 2 s, and the discrepancy between PINN prediction and analytical solution is less than 0.9%. To further prove the interpolation ability of the PINN scheme, Fig. 2C shows the dimensionless thermal conductivity ( $k_{eff}/k_{bulk}$ , where  $k_{eff} = qL/\Delta T$  and  $k_{bulk} = \frac{1}{3} \sum_p \int_0^{\omega_{max,p}} C|v|^2 \tau d\omega$ ) at both seen and unseen characteristic lengths (the filled circle represents the seen lengths while the open circle represents the unseen lengths), and the comparison with the analytical solution. It is observed that PINN can provide accurate predictions within the training domain (i.e., the range of characteristic length used for training) due to its interpolation ability, and thereby achieve the learning of parametric solutions.

### 3.1.2 2D phonon transport

In addition to the 1D case, the PINN scheme is also validated in a 2D simulation. The system is depicted in Fig. 3A, with periodic boundary

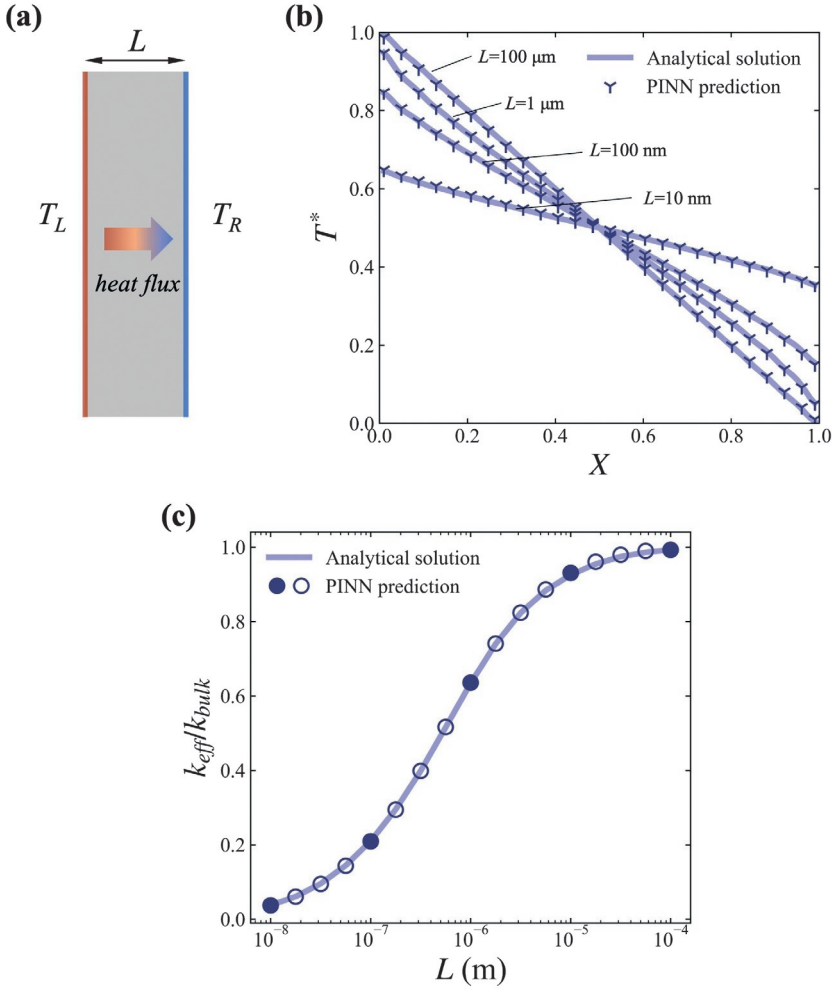


**Fig. 2** Results of a 1D cross-plane phonon transport simulation. (A) Schematic of the 1D cross-plane phonon transport case. (B) Dimensionless temperature profiles of silicon thin films with different thicknesses. (C) Effective thermal conductivity normalized by the bulk thermal conductivity at different film thicknesses.

conditions applied on the left and right sides and adiabatic boundary conditions applied on the top and bottom sides. The distance between the top and bottom boundaries is  $H$ , which is also selected as one of the training features to enable parametric learning. In this model,  $H$  ranges between 10 nm and 100  $\mu\text{m}$ , and the PINN scheme can predict temperature and heat flux within this range after training.

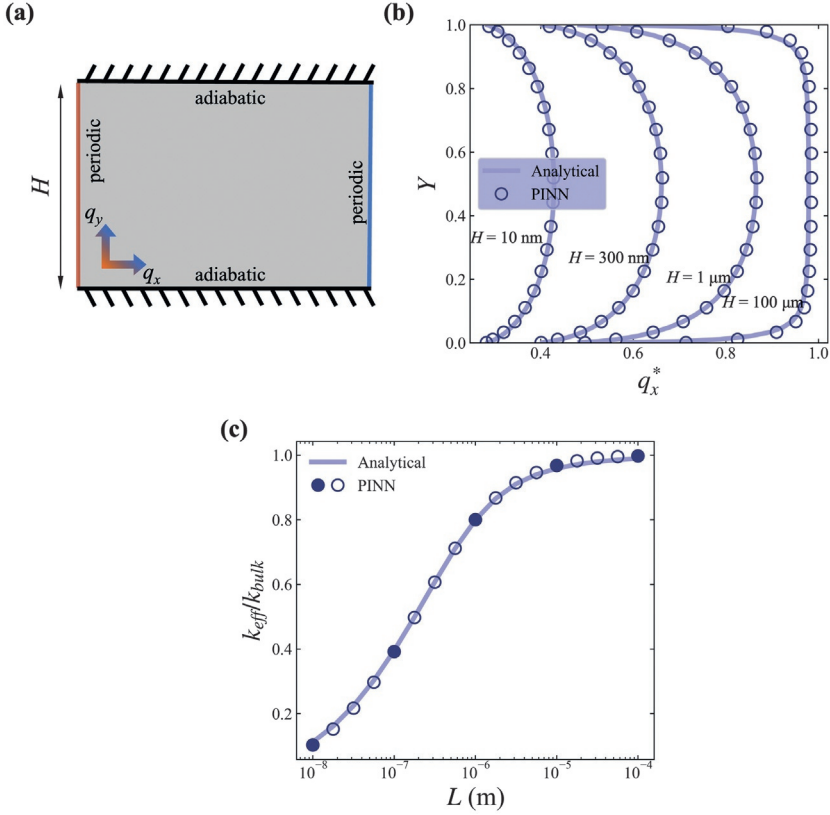


**Fig. 3** Results of a 2D in-plane phonon transport simulation. (A) Schematic of the 2D in-plane phonon transport case. (B) Distribution of dimensionless x-directional heat flux  $q_x^*$  along the y-axis in thin films with different thicknesses. (C) Effective thermal conductivity normalized by the bulk thermal conductivity at different length scales.

Fig. 3B shows the dimensionless heat flux ( $q_x^* = q_x(Y)/q_{bulk}$ ) profile along the x direction under different lengths (i.e.,  $H$ 's). By comparing to the analytical solution derived from the Fuchs-Sondheimer theory [31], the PINN scheme is validated to be capable of tackling 2D thermal transport problems (error less than 2.4% in this problem) within a wide range of characteristic lengths. To further validate the interpolation ability, dimensionless thermal conductivity is compared to the analytical solution under both seen and unseen length scales, and they achieve good accuracy (error less than 1.6%).

Another 2D case is also studied based on the PINN scheme. A square domain with side length  $L$  and four isothermal boundary conditions is adopted, with the top boundary maintained at high temperature  $T_h$  and other boundaries maintained at low temperature  $T_c$ , as depicted in Fig. 4A.

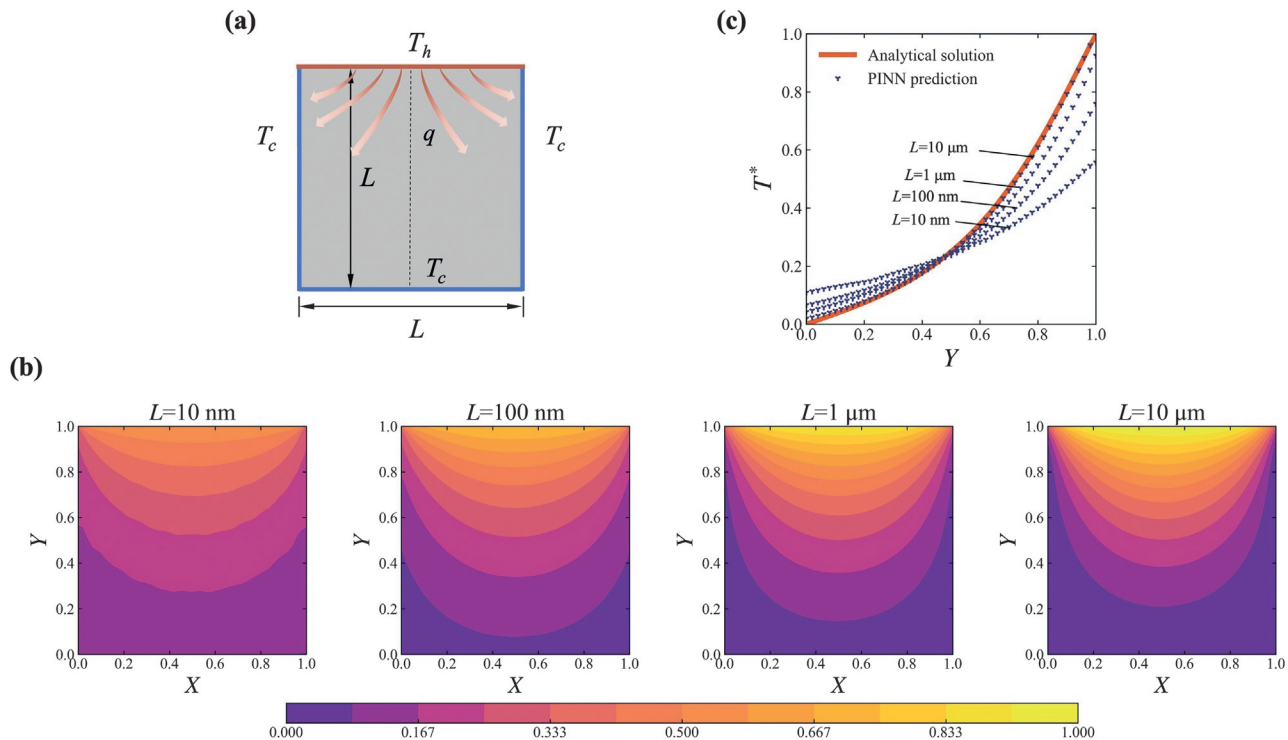


**Fig. 4** Results of a 2D square phonon transport simulation. (A) Schematic of the 2D square phonon transport case. (B) Contours of dimensionless steady-state temperature at different length scales.  $X$  and  $Y$  are the normalized spatial coordinates. (C) Non-dimensional temperature profiles along the vertical centerline.

The temperature difference is  $\Delta T = T_h - T_c = 1$  K. Similarly, training is performed on different length scales ranging from 10 nm to 10  $\mu\text{m}$ . Fig. 4B shows the dimensional temperature contour at different length scales. Although there is no available benchmark to compare directly, the study shows the temperature profile along the vertical centerline at  $x = 0.5L$ , and compares it with Fourier's law in the diffusive limit (i.e., 10  $\mu\text{m}$ , which is much larger than phonon mean free path in silicon (about 300 nm)). As shown in Fig. 4C, the non-dimensional temperature along the vertical centerline converges to the analytical solution of Fourier's law as the characteristic length increases.

### 3.1.3 3D phonon transport

For practical applications, thermal transport problems cannot always be reduced to 1D or 2D geometries, but they need to be treated in full 3D, which requires extending the PINN scheme to 3D in order to solve real-world problems. To prove the PINN's ability to do so, a 3D silicon block of dimensions  $L \times L \times 0.5L$ , with isothermal boundary conditions is studied. On the top surface, a circular hot spot of Gaussian temperature distribution (standard deviation  $= L/6$ ) is adopted, with the temperature remaining at the highest  $T_h$  at the center and gradually decaying to  $T_c$  when approaching the boundaries. On the other surfaces, the temperature remains at  $T_c$ . This setup simulates a Gaussian laser spot heating up the sample surface, as shown in Fig. 5A. Training is performed on two PINNs to handle different length-scale thermal transport problems separately. Specifically, one PINN is used for  $L$  ranging between 10 nm to 1  $\mu\text{m}$ , and the other is for  $L$  ranging between 10  $\mu\text{m}$  and 1 mm. Splitting the training can benefit the training accuracy by reducing the number of collocation points. The phonon energy distribution is more isotropic in larger length scales, and as a result, fewer discrete points are required to achieve accurate results.

Contours of dimensionless steady-state temperature under different characteristic lengths are shown in Fig. 5B–F. Due to the lack of solutions to mode-resolved 3D phonon BTE, the result is compared with Fourier's law in the diffusive limit for validation. In particular, a simple PINN scheme is adopted to obtain the solution to the 3D heat equation with the same boundary setup, as shown in Fig. 5G. Comparing the PINN prediction in Fig. 5F with the result obtained by Fourier's law, the error is less than 1.4%. For Section 3.1, training and testing information is summarized in Table A1, and training and validation losses are summarized in Table A2.

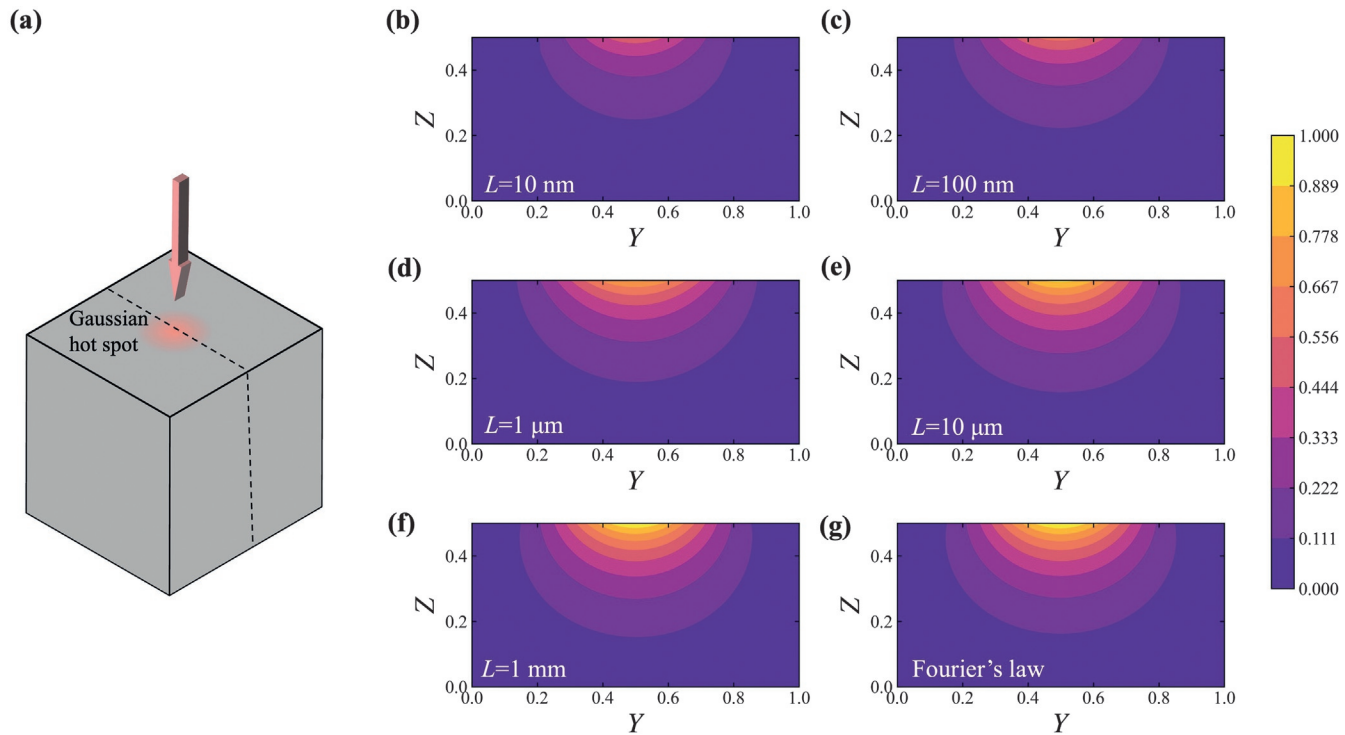


**Fig. 5** Results of the 3D cuboid phonon transport simulation. (A) Schematic of the 3D cuboid phonon transport case. (B–F) PINN-predicted contours of dimensionless steady-state temperature in the central plane. (G) Benchmark result of Fourier's law in the diffusive limit.

**Table A1** Training and testing information in solving steady-state phonon BTE under a small temperature difference.

Case	Training				Testing			
	$N_x$	$N_y$	$N_z$	Walltime (h)	$N_x$	$N_y$	$N_z$	Walltime (s) $L$ (m)
1D cross-plane	40	16	5	0.80	40	64	17	2.11 $[10^{-8}, 10^{-4}]$
2D in-plane	300	144	5	4.83	1600	1024	17	24.72 $[10^{-8}, 10^{-4}]$
2D square	450	144	4	6.62	2601	576	7	9.57 $[10^{-8}, 10^{-5}]$
3D cuboid <sup>a</sup>	1200	144	3	15.52	132651	576	5	344.54 $[10^{-8}, 10^{-6}]$
3D cuboid <sup>b</sup>	1200	64	3	8.68	132651	576	5	351.64 $[10^{-5}, 10^{-3}]$

**Table A2** Training and validation losses in solving steady-state phonon BTE under a small temperature difference.

Case	Training loss	Validation loss
1D cross-plane	$2.0 \times 10^{-4}$	$1.4 \times 10^{-3}$
2D in-plane	$5.6 \times 10^{-4}$	$4.5 \times 10^{-3}$
2D square	$2.4 \times 10^{-2}$	$1.6 \times 10^{-2}$
3D cuboid <sup>a</sup>	$6.5 \times 10^{-3}$	$8.8 \times 10^{-3}$
3D cuboid <sup>b</sup>	$9.8 \times 10^{-3}$	$4.9 \times 10^{-3}$

### 3.2 Solve steady-state phonon BTE under arbitrary temperature differences

In the last section, a small temperature difference is assumed so that the energy term in the phonon BTE can be linearized (Eq. 3). However, in many practical applications, the small temperature difference assumption may not hold. For example, when a high-intensity laser heats up a metal surface, the local hot spot temperature can be much higher than the rest of the metal. In power electronics, the hot spot near the gate region can be tens of degrees higher than the rest of the package [32]. A finite-volume discrete unified gas kinetic scheme is developed to extend the numerical solver to tackle phonon transport problems with arbitrary temperature differences [33]. To generalize the PINN model and make it applicable to cases with large temperature differences, one needs to adopt the distribution function  $f$ -based phonon BTE with a space-dependent relaxation time which is determined by the local temperature [28,33]. Under SMRT approximation, the steady-state mode-resolved phonon BTE can be written as,



$$\boldsymbol{\nu} \cdot \nabla f = \frac{f^{eq}(T) - f}{\tau(T)} \quad (10)$$

The phonon distribution function  $f = f(\mathbf{x}, \mathbf{s}, k, p)$  (or  $f(\mathbf{x}, \mathbf{s}, \omega, p)$ ) is a function determined by spatial vector  $\mathbf{x}$ , directional unit vector  $\mathbf{s} = (\cos\theta, \sin\theta\cos\varphi, \sin\theta\sin\varphi)$  ( $\theta$  is the polar angle and  $\varphi$  is the azimuthal angle), wave number  $k$  (or angular frequency  $\omega = \omega(k, p)$ ) and polarization  $p$ . The phonon equilibrium distribution function  $f^{eq}$  follows the Bose-Einstein distribution, as shown in Eq. (2). Compared to the last section where a small temperature difference assumption was made, effective phonon relaxation time  $\tau(\omega, p, T)$  not only depends on frequency  $\omega$  and polarization  $p$ , but also depends on the local temperature  $T$ . Similarly, Eq. (11) should be satisfied due to the energy conservation of the scattering term,

$$\nabla \cdot \mathbf{q} = \sum_p \int_0^{\omega_{\max,p}} \int_{4\pi} \hbar\omega D \frac{f^{eq}(T) - f}{\tau(T)} d\Omega d\omega = 0 \quad (11)$$

where the heat flux  $\mathbf{q}$  is defined in Eq. (12).

$$\mathbf{q} = \sum_p \int_0^{\omega_{\max,p}} \int_{4\pi} \boldsymbol{\nu} \hbar\omega D f d\Omega d\omega \quad (12)$$

Similar to the previous structure, two fully connected DNNs are adopted to approximate the equilibrium phonon distribution function  $f^{eq}(T)$  and equilibrium phonon distribution function  $f^{neq}(T) = f - f^{eq}(T)$  separately, as shown in Fig. 6. The inputs to the neural networks are position vector  $\mathbf{x}$  (including  $x$ ,  $y$ , and  $z$ ), solid angle  $\mathbf{s}$ , wave number  $k$ , polarization  $p$ , and additional parameters  $\boldsymbol{\mu}$ . Here,  $\boldsymbol{\mu}$  is set to be either characteristic length  $L$  or boundary temperature difference  $\Delta T$ , but it can be extended to other physical parameters. Each sub-network maps those input parameters to a target label (i.e.,  $f^{eq}(T)$  or  $f^{neq}(T)$ ). It is noted that one of the outputs from the DNNs is local equilibrium temperature  $T$ , which further determines  $f^{eq}(T)$  and  $\tau(T)$ . Combining  $f^{eq}(T)$  and  $f^{neq}(T)$  yields the phonon distribution function  $f$ , which is plugged into Eq. (10) to form the first part of the residual. The second part of the residual comes from Eq. (11), which is hard to evaluate and proper nondimensionalization must be performed. Inspired by the way to tackle small temperature differences, a pretrained shallow neural network with only one hidden layer is adopted to approximate the coefficient  $\beta(T)$  as shown in Eq. (13),

$$f^{eq}(T) \approx f^{eq}(T_{ref}) + \beta(T)(T^* - T_{ref}) \quad (13)$$

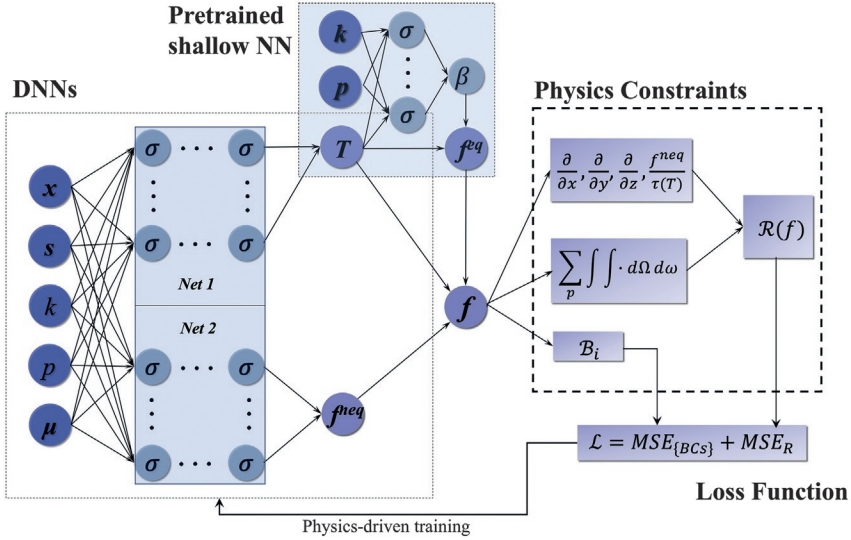


**Fig. 6** A schematic of the PINN framework for solving stationary mode-resolved phonon BTE with arbitrary temperature differences.

where  $T^*$  is the same as  $T$ . Plugging Eq. (13) into Eq. (11) yields the local temperature,

$$T^* = T_{ref} + \frac{1}{4\pi} \left( \sum_p \int_0^{\omega_{max,p}} \int_{4\pi} \hbar \omega D \frac{f - f^{eq}(T)}{\tau(T)} d\Omega d\omega \right) \quad (14)$$

$$\times \left( \sum_p \int_0^{\omega_{max,p}} \frac{\hbar \omega D \beta(T)}{\tau(T)} d\omega \right)^{-1}$$

where  $T^* = T$  should be satisfied and serve as the second part of the residual. Eq. (15) shows the composition of the residual from the laws of physics.

$$\mathcal{R}(f(\mathbf{x}, s, k, p, \boldsymbol{\mu}), T) = \begin{cases} \boldsymbol{\nu} \cdot \nabla f - \frac{f^{eq}(T) - f}{\tau(T)} = 0 & \mathbf{x}, s, k, p \in \Gamma, \boldsymbol{\mu} \in \mathbb{R}^d \\ T^* - T = 0, \end{cases} \quad (15)$$

As a result, the PINNs are trained by minimizing the loss function defined below,

$$\mathcal{L} = \left\| \boldsymbol{\nu} \cdot \nabla f - \frac{f^{eq}(T) - f}{\tau(T)} \right\|^2 + \|T^* - T\|^2 + \sum_i \|\mathcal{B}_i\|^2, \quad (16)$$

where  $\mathcal{B}_i$  are operators that define various boundary conditions.

### 3.2.1 1D phonon transport

To validate the proposed scheme, numerical tests on a 1D cross-plane thermal transport problem in silicon thin films are performed. This problem is described by 1D  $f$ -based phonon BTE, with two isothermal boundary conditions. Generally, the system setup is the same as that in Section 3.1.1, except for the magnitude of the temperature difference across the domain.

In the diffusive limit where thickness  $L$  is much larger than the phonon mean free path (as depicted in Fig. 7A), Fourier's law can be applied to describe heat conduction even if the temperature difference across the material is large as long as the local thermal conductivity is treated as temperature-dependent. Therefore, the scheme is tested near the diffusive limit and

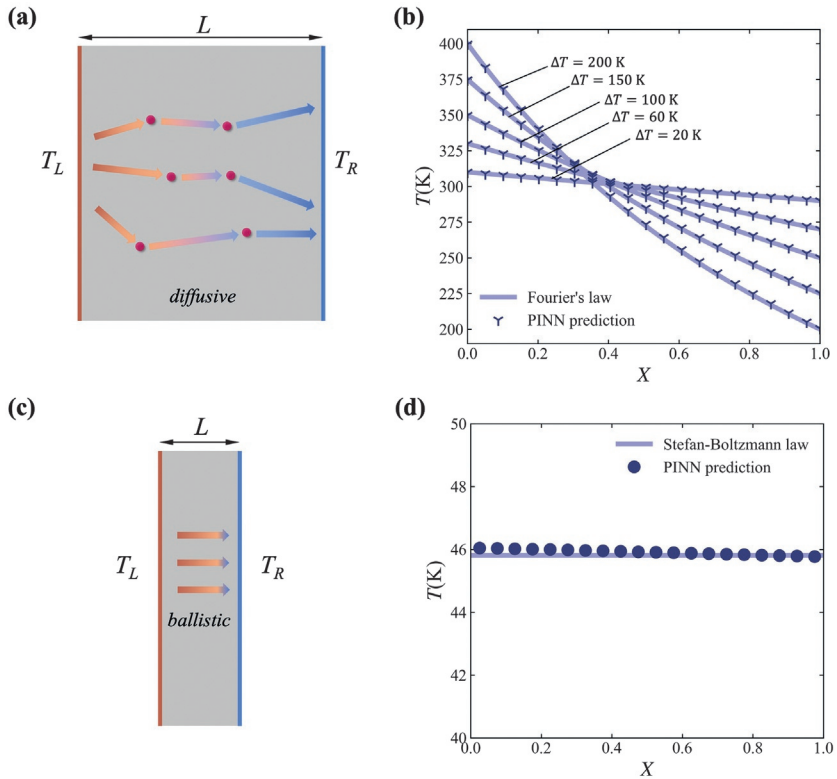


**Fig. 7** Results of 1D cross-plane phonon transport in the diffusive and ballistic limits with arbitrary temperature differences. (A) Schematic of 1D cross-plane diffusive phonon transport. (B) Temperature profiles under different temperature differences in the diffusive limit. The solid line is the analytical solution of Fourier's law. (C) Schematic of 1D cross-plane ballistic phonon transport. (D) Temperature profiles in the ballistic limit. The solid line is the analytical solution of Stefan-Boltzmann law.

compared with the results derived by Fourier's law for the purpose of validation. To achieve fast prediction under different temperature differences,  $\Delta T$  is selected as the additional training parameter  $\mu$  as mentioned before. In particular, the shallow NN is trained in the relevant temperature range to generate  $\beta$ , and then the PINN model is trained on five sampled temperature differences ( $\Delta T = 20, 60, 100, 150$ , and  $200$  K,  $T_{ref} = 300$  K) at a fixed thickness  $L$  ( $100 \mu\text{m}$ ). Then, the predicted results by the PINN model are compared with analytical solutions of Fourier's law, as shown in Fig. 7B. It is noted that the predicted results agree almost exactly with the analytical solutions, with the mean absolute error less than  $0.4$  K.

In the ballistic limit where thickness  $L$  is much smaller than the phonon mean free path (as depicted in Fig. 7C), phonon transport is governed by Stefan-Boltzmann law [34]. In this case,  $L$  is chosen to be  $10$  nm such that phonon scattering is rare, and the temperature profile approximately follows  $T^4 = (T_L^4 - T_R^4)/2$ . The temperature on the left boundary  $T_L$  is maintained at  $50$  K, and the temperature on the right boundary  $T_R$  is maintained at  $40$  K. Fig. 7D shows the comparison between the predicted temperature profile and the analytical solution derived by Stefan-Boltzmann law. The local temperature in-between two boundaries does not have significant change in the spatial domain, because of the low phonon scattering rate. It shows that the predicted results agree well with the Stefan-Boltzmann law, and the little discrepancy originates from the fact that some short mean free path phonons get scattered no matter how small the characteristic length is.

### 3.2.2 2D phonon transport

To further validate the PINN scheme on higher-dimension thermal transport problems, heat conduction in a 2D rectangular domain ( $L$  by  $0.5L$ , as depicted in Fig. 8A) with four isothermal boundary conditions is evaluated. The temperature profile on the top boundary follows Gaussian distribution  $T_h$ , with the full width at half maximum (FWHM) to be  $0.4L$ . Other boundaries are held at a lower temperature  $T_c = 300$  K, and the difference between  $T_c$  and the maximum temperature on the top boundary  $T_{max}$  is set to be  $100$  K. To achieve parametric learning, the characteristic length scale  $L$  is set to be the additional training parameter  $\mu$ . In particular, four sampled  $L$  values ranging from  $100$  nm to  $100 \mu\text{m}$  are adopted. Fig. 8 B–D show the predicted temperature contour in the 2D rectangular domain, which successfully reproduce the Gaussian temperature profiles on the top boundaries. Fig. 8E shows the temperature contour calculated based on a simple PINN model which solves the 2D steady-state heat equation (Fourier's law).

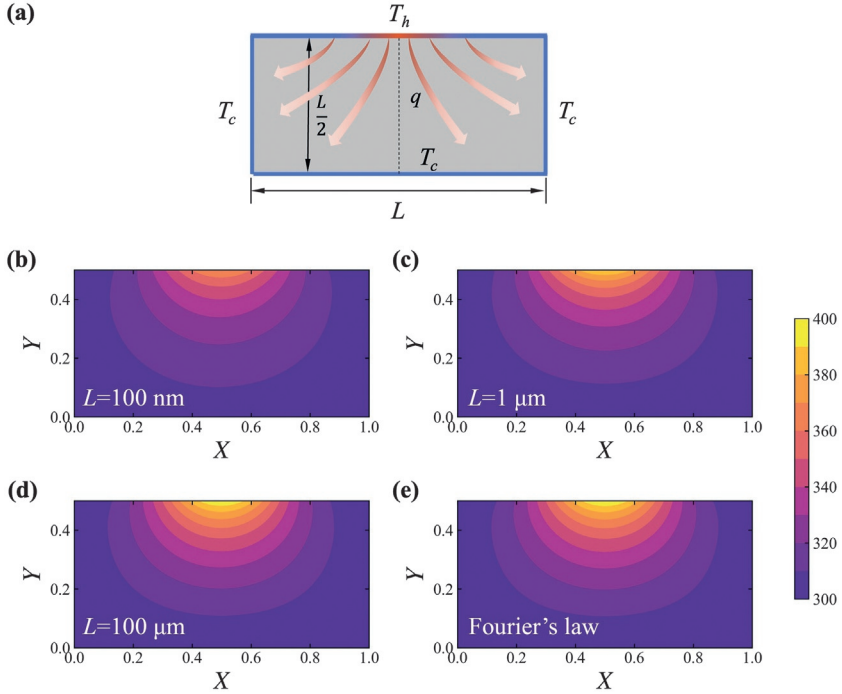


**Fig. 8** Results of 2D rectangular phonon transport problem under a large temperature difference. (A) Schematic of 2D phonon transport in a rectangular domain. (B–D) Contours of dimensionless steady-state temperature at different length scales.  $X$  and  $Y$  are the normalized spatial coordinates. (E) Benchmark result of Fourier's law in the diffusive limit.

It serves as the benchmark result because the phonon BTE converges to Fourier's law in the diffusive limit, and there is no available analytical solution of 2D mode-resolved phonon BTE for direct comparison. It is observed that Fig. 8D ( $L=100$   $\mu$ m) is almost identical to Fig. 8E, with the mean absolute error less than 0.3 K. Therefore, it confirms that the PINN scheme can provide accurate predictions in the 2D heat conduction problems with large temperature differences.

### 3.2.3 3D phonon transport

To handle the more realistic heat conduction problems, phonon BTE is solved for a 3D cuboid geometry, with isothermal boundary conditions applied on all surfaces. Generally, the system setup is the same as the setup used in Section 3.1.3, except for the amplitude of temperature difference. The peak temperature on the top surface  $T_{max}$  is set to be 200 K (at the center

of the 2D Gaussian distribution with FWHM to be  $0.4L$ ), and the temperature on the other surfaces is maintained at  $T_c=100$  K. The characteristic length is chosen as 1 mm to enable the comparison with Fourier’s law in the diffusive limit. Similar to the previous test, this simulation compares the PINN-predicted result with Fourier’s law in the diffusive limit (as shown in Fig. 9), and the mean absolute temperature difference is less than 0.2 K. For Section 3.2, training and testing information is summarized in Table A3, and training and validation losses are summarized in Table A4.

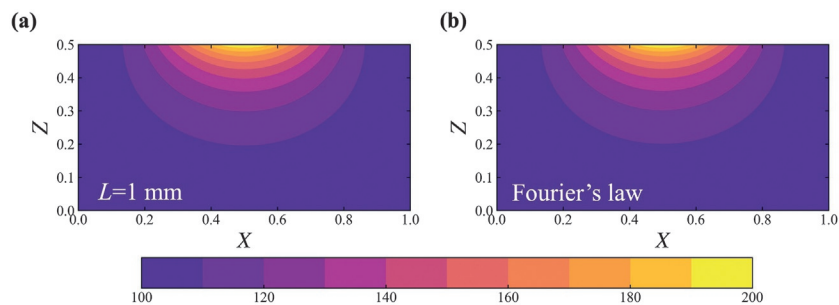


**Fig. 9** Results of 3D phonon transport problem under a large temperature difference. (A) PINN-predicted contours of steady-state temperature in the central plane. (B) Benchmark result of Fourier’s law in the diffusive limit.

**Table A3** Training and testing information in solving steady-state phonon BTE under arbitrary temperature differences.

Case	Training				Testing				$\mu$	Range of $\mu$
	$N_x$	$N_z$	$N_\mu$	Walltime (h)	$N_x$	$N_z$	$N_\mu$	Walltime (s)		
1D cross-plane	40	16	5	0.38	80	64	5	0.05	$\Delta T$ (K)	[200, 400]
2D rectangle	450	100	4	3.46	2601	576	4	5.79	$L$ (m)	$[10^{-7}, 10^{-4}]$
3D cuboid	1600	100	3	11.13	132,651	576	4	301.26	$L$ (m)	$[3 \times 10^{-7}, 3 \times 10^{-6}]$

**Table A4** Training and validation losses in solving steady-state phonon BTE under arbitrary temperature differences.

Case	Training loss	Validation loss
1D cross-plane	$1.0 \times 10^{-4}$	$6.5 \times 10^{-4}$
2D rectangle	$8.5 \times 10^{-3}$	$9.7 \times 10^{-3}$
3D cuboid	$8.0 \times 10^{-3}$	$1.0 \times 10^{-2}$

### 3.3 Solve transient phonon BTE

In many real-world applications, non-steady thermal processes are of great importance, which emphasizes the necessity of studying transient phonon BTE. The time-dependent phonon BTE gray model is first studied. In the gray model, all phonon modes are assumed to have the same properties. To some extent, the gray model can provide some insightful predictions on the phonon transport behaviors, including ballistic and boundary scattering effects [35].

The laser-induced transient thermal grating (TTG) process is modeled for testing the PINN scheme. TTG permits non-contact measurements of thermal conductivity on nanostructured samples, without the need for metal heaters or any other extraneous structures [36]. Here, the thermal relaxation process of a 1D TTG is considered, where initially two crossed laser pulses are imposed to generate a spatially sinusoidal temperature variation due to interference across a silicon thin film [37]. The initial condition and boundary condition are illustrated in Eq. (17),

$$\begin{cases} T(x, 0) = T_{ref} + A_0 \cos\left(\frac{2\pi x}{L}\right) \\ T(0, t) = T(L, t) \end{cases} \quad (17)$$

where the periodic boundary condition is applied. The energy term of the phonon BTE can be linearized since the pulse is weak, thus the temperature difference is small compared to the mean temperature. The temperature deviation from the reference temperature,  $\Delta T = T - T_{ref}$ , can be approximated as  $\Delta T = A(t) \cos\left(\frac{2\pi x}{L}\right)$ , where  $A(t)$  is the amplitude of the temperature variation, and it can be obtained analytically [37],

$$\hat{A}(t^*) = \text{sinc}(\xi t^*)e^{-t^*} + \int_0^{t^*} \hat{A}(t') \text{sinc}[\xi(t' - t^*)] e^{(t' - t^*)} dt' \quad (18)$$

where  $\hat{A} = A/A_0$ ,  $t^* = t/\tau$ , and the rarefaction parameter  $\xi = 2\pi Kn$ .

As shown in Fig. 10, the previously derived PINN framework is modified to predict the thermal relaxation process of the 1D TTG process. The major difference is that time,  $t$ , is added as an input parameter. The rarefaction parameter is chosen to be 1, and the training time domain is taken to be twice the phonon relaxation time. After training, the temperature can be evaluated at new locations and times, given the interpolation ability of DNNs. Fig. 11A shows the schematic of the 1D silicon thin film, where

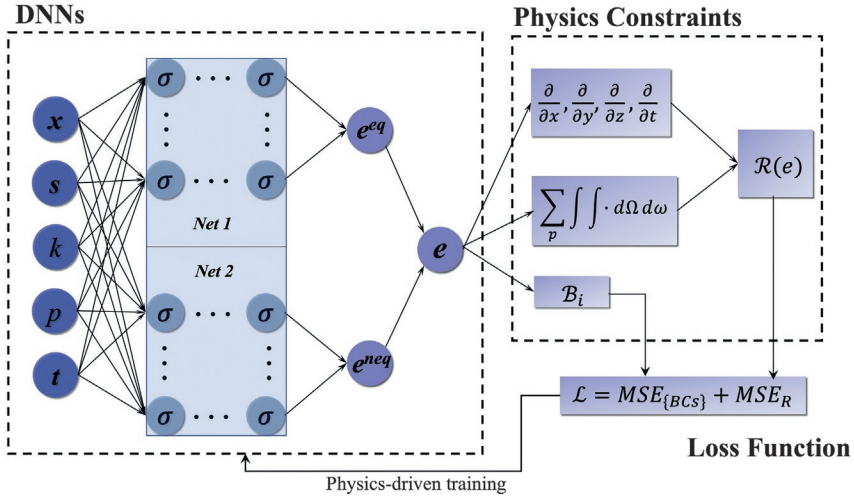


**Fig. 10** A schematic of PINN framework for solving transient phonon BTE.

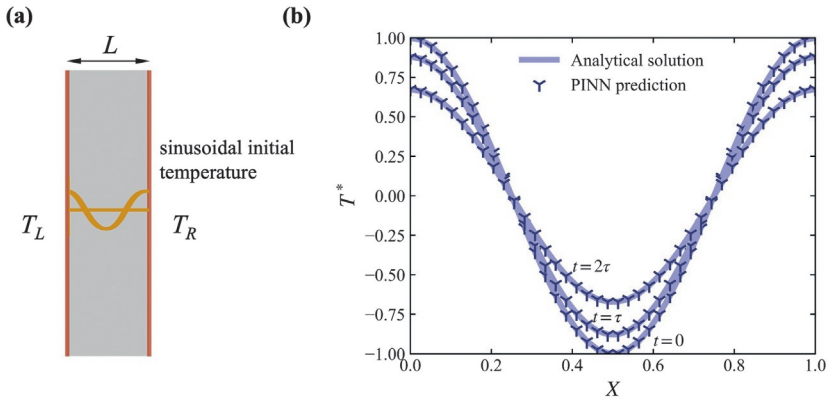


**Fig. 11** Results of the 1D thermal grating (gray model). (A) Schematic of the 1D cross-plane transient phonon transport. (B) Temperature deviation  $T^*$  validated by analytical solution at  $t = 0$ ,  $t = \tau$ , and  $t = 2\tau$ .  $X$  is the normalized coordinate.

a sinusoidal initial temperature is applied. The results are compared with the analytical solutions obtained by the method of degenerate kernels [30], as shown in Fig. 11B, with PINN results in red dashed lines and analytical solution in black solid line. PINN results show good agreement with the analytical solution, which shows the PINN's capability of capturing transient phonon transport.





## 4. Conclusion and perspective

In summary, a PINN-based scheme is shown capable of solving the phonon Boltzmann transport equation accurately and efficiently. In particular, the PINN scheme is successfully applied to solve 1D, 2D, and 3D thermal transport problems under small temperature differences, and it can be modified to tackle similar problems but under arbitrary temperature differences by incorporating a pre-trained shallow neural network into the scheme. Furthermore, transient phonon BTE (gray model) is also solved by including time  $t$  in the PINN input layer. All of these cases achieve high accuracy and efficiency. Training and testing information is included in the [Appendix](#). It is noted that the training can be performed in a parametric setting, allowing a trained model to quickly evaluate the thermal transport of structures with different geometries, dimensions, and temperature differences.

Although efficiently solving the phonon BTE has already been achieved, the training efficiency can be further improved by modifying the PINN structure to impose physical constraints in a hard manner, instead of encapsulating everything directly into the loss function. Convolutional neural network (CNN) could be applied to solve problems in irregular geometries [38], and by leveraging the parameter sharing feature of CNN we can expect faster training compared to the current PINN design. Moreover, the proposed PINN scheme may also be further developed to solve thermal transport problems that involve multiple materials and interfaces by incorporating interfacial phonon transport properties into the existing scheme. Additionally, by taking into account mode-resolved phonon and electron properties and using a set of BTEs with the electron-phonon interaction being the coupling term, coupled phonon and electron transport can be investigated based on the PINN scheme, which would be the ultimate tool to simultaneously model electrical and thermal performances that are interdependent. Importantly, PINN-based phonon BTE solver may also be interfaced with first-principles density-functional theory (DFT) calculations, molecular dynamics (MD) simulations, and Fourier's law to form an integrated solver that can handle multiscale thermal transport problems. In such a scenario, DFT or MD simulations can provide critical phonon properties, such as mode-resolved phonon relaxation times and interfacial phonon transmission coefficients, to the phonon BTE to solve thermal transport problems in realistic devices [39].

Nowadays, the increased integration and miniaturization of electronic devices leads to serious self-heating problems. The ability to predict thermal transport accurately and efficiently and to infer the temperature and hot spots of a complicated electronic device will be instrumental to its initial design and health monitoring during operation. Based on the PINN scheme discussed in this chapter, new machine learning techniques can be developed for multiscale, multi-material thermal modeling, which may open pathways for device design optimization by taking into account non-diffusive transport effects and phonon-electron coupling.



## Appendix

Numerical experiments are performed on a NVIDIA GeForce TITAN Xp GPU for Sections 3.1 and 3.3, and on a NVIDIA Tesla P100 GPU for Section 3.2 (Table A1–A4).

$N_x$ ,  $N_s$ , and  $N_t$  denote the number of sampled points in the spatial domain, the number of sampling points in the solid angle space, and the number of selected characteristic lengths, separately. The superscripts “a” and “b” denote the two different models trained for 3D geometries with different ranges of length scale  $L$ .

For solving transient phonon BTE,  $N_x = 40$ ,  $N_s = 16$ ,  $N_t = 40$ , where  $N_t$  is the number of sampled points in the time domain. The training process takes 82.68 s, while the testing process takes  $6.6 \times 10^{-3}$  s. The training loss is  $9.0 \times 10^{-6}$ .

## References

- [1] G. Jiang, L. Diao, K. Kuang, *Advanced Thermal Management Materials*, Springer New York, New York, NY, 2013, <https://doi.org/10.1007/978-1-4614-1963-1>.
- [2] C.L. Tien, *Microscale Energy Transfer*, CRC Press, 1997.
- [3] R. Peierls, Zur kinetischen theorie der wärmeleitung in kristallen, *Ann. Phys.* 395 (1929) 1055–1101.
- [4] G. Chen, *Nanoscale Energy Transport and Conversion: A Parallel Treatment of Electrons, Molecules, Phonons, and Photons*, Oxford University Press, 2005.
- [5] A.J. Minnich, G. Chen, S. Mansoor, B.S. Yilbas, Quasiballistic heat transfer studied using the frequency-dependent Boltzmann transport equation, *Phys. Rev. B.* 84 (2011) 235207, <https://doi.org/10.1103/PhysRevB.84.235207>.
- [6] J.M. Loy, S.R. Mathur, J.Y. Murthy, A coupled ordinates method for convergence acceleration of the phonon Boltzmann transport equation, *J. Heat Transfer* 137 (2015) 012402.
- [7] M.L. Adams, E.W. Larsen, Fast iterative methods for discrete-ordinates particle transport calculations, *Prog. Nucl. Energy.* 40 (2002) 3–159.

- [8] C. Zhang, Z. Guo, S. Chen, An implicit kinetic scheme for multiscale heat transfer problem accounting for phonon dispersion and polarization, *Int. J. Heat Mass Transf.* 130 (2019) 1366–1376.
- [9] S.A. Ali, G. Kollu, S. Mazumder, P. Sadayappan, A. Mittal, Large-scale parallel computation of the phonon Boltzmann transport equation, *Int. J. Therm. Sci.* 86 (2014) 341–351.
- [10] A. Voulodimos, N. Doulamis, A. Doulamis, E. Protopapadakis, Deep learning for computer vision: a brief review, *Comput. Intell. Neurosci.* 2018 (2018) 7068349.
- [11] B.A. Richards, T.P. Lillicrap, P. Beaudoin, Y. Bengio, R. Bogacz, A. Christensen, C. Clopath, R.P. Costa, A. de Berker, S. Ganguli, A deep learning framework for neuroscience, *Nat. Neurosci.* 22 (2019) 1761–1770.
- [12] T. Young, D. Hazarika, S. Poria, E. Cambria, Recent trends in deep learning based natural language processing, *IEEE Comput. Intell. Mag.* 13 (2018) 55–75.
- [13] J. Han, A. Jentzen, E. Weinan, Solving high-dimensional partial differential equations using deep learning, *Proc. Natl. Acad. Sci. U. S. A.* 115 (2018) 8505–8510, <https://doi.org/10.1073/pnas.1718942115>.
- [14] J. Lu, Z. Shen, H. Yang, S. Zhang, Deep network approximation for smooth functions, *SIAM J. Math. Anal.* 53 (2021) 5465–5506.
- [15] M. Hutzenthaler, A. Jentzen, T. Kruse, T.A. Nguyen, A proof that rectified deep neural networks overcome the curse of dimensionality in the numerical approximation of semilinear heat equations, *SN Partial Differ. Equ. Appl.* 1 (2020) 10, <https://doi.org/10.1007/s42985-019-0006-9>.
- [16] M. Raissi, P. Perdikaris, G.E. Karniadakis, Physics-informed neural networks: a deep learning framework for solving forward and inverse problems involving nonlinear partial differential equations, *J. Comput. Phys.* 378 (2019) 686–707.
- [17] X.I.A. Yang, S. Zafar, J.-X. Wang, H. Xiao, Predictive large-eddy-simulation wall modeling via physics-informed neural networks, *Phys. Rev. Fluids.* 4 (2019), 034602.
- [18] Z. Mao, A.D. Jagtap, G.E. Karniadakis, Physics-informed neural networks for high-speed flows, *Comput. Methods Appl. Mech. Eng.* 360 (2020) 112789, <https://doi.org/10.1016/j.cma.2019.112789>.
- [19] L. Sun, H. Gao, S. Pan, J.-X. Wang, Surrogate modeling for fluid flows based on physics-constrained deep learning without simulation data, *Comput. Methods Appl. Mech. Eng.* 361 (2020) 112732, <https://doi.org/10.1016/j.cma.2019.112732>.
- [20] M. Raissi, A. Yazdani, G.E. Karniadakis, Hidden fluid mechanics: learning velocity and pressure fields from flow visualizations, *Science* 367 (2020) 1026–1030, <https://doi.org/10.1126/science.aaw4741>.
- [21] S. Cai, Z. Wang, S. Wang, P. Perdikaris, G.E. Karniadakis, Physics-informed neural networks for heat transfer problems, *J. Heat Transfer* 143 (2021) 060801.
- [22] V. Oommen, B. Srinivasan, Solving inverse heat transfer problems without surrogate models: a fast, data-sparse, physics informed neural network approach, *J. Comput. Inf. Sci. Eng.* 22 (2022) 041012.
- [23] S. Liao, T. Xue, J. Jeong, S. Webster, K. Ehmann, J. Cao, Hybrid Full-Field Thermal Characterization of Additive Manufacturing Processes Using Physics-Informed Neural Networks With Data, 2022, <https://doi.org/10.48550/ARXIV.2206.07756>.
- [24] S. Mishra, R. Molinaro, Physics informed neural networks for simulating radiative transfer, *J. Quant. Spectrosc. Radiat. Transf.* 270 (2021) 107705.
- [25] Y. Bai, T. Chaolu, S. Bilge, The application of improved physics-informed neural network (IPINN) method in finance, *Nonlinear Dyn.* 107 (2022) 3655–3667.
- [26] T.M. Razakh, B. Wang, S. Jackson, R.K. Kalia, A. Nakano, K. Nomura, P. Vashishta, PND: physics-informed neural-network software for molecular dynamics applications, *Software X.* 15 (2021) 100789.

- [27] X. Jiang, D. Wang, Q. Fan, M. Zhang, C. Lu, A.P.T. Lau, Physics-informed neural network for nonlinear dynamics in Fiber optics, *Laser Photonics Rev.* 16 (2022) 2100483.
- [28] R. Li, J.-X. Wang, E. Lee, T. Luo, Physics-informed deep learning for solving phonon Boltzmann transport equation with large temperature non-equilibrium, *NPJ Comput. Mater.* 8 (2022) 29, <https://doi.org/10.1038/s41524-022-00712-y>.
- [29] R. Li, E. Lee, T. Luo, Physics-informed neural networks for solving multiscale mode-resolved phonon Boltzmann transport equation, *Mater. Today Phys.* 19 (2021) 100429.
- [30] C. Hua, A.J. Minnich, Semi-analytical solution to the frequency-dependent Boltzmann transport equation for cross-plane heat conduction in thin films, *J. Appl. Phys.* 117 (2015) 175306.
- [31] J. Cuffe, J.K. Eliason, A.A. Maznev, K.C. Collins, J.A. Johnson, A. Schepetov, M. Prunnila, J. Ahopelto, C.M. Sotomayor Torres, G. Chen, K.A. Nelson, Reconstructing phonon mean-free-path contributions to thermal conductivity using nanoscale membranes, *Phys. Rev. B* 91 (2015) 245423, <https://doi.org/10.1103/PhysRevB.91.245423>.
- [32] J. Cho, Z. Li, M. Asheghi, K.E. Goodson, Near-junction thermal management: Thermal conduction in gallium nitride composite substrates, *Annu. Rev. Heat Transf.* 18 (2015) 7–45.
- [33] C. Zhang, Z. Guo, Discrete unified gas kinetic scheme for multiscale heat transfer with arbitrary temperature difference, *Int. J. Heat Mass Transf.* 134 (2019) 1127–1136.
- [34] A. Majumdar, Microscale heat conduction in dielectric thin films, *J. Heat Transfer* 115 (1993) 7–16.
- [35] C. Zhang, Z. Guo, S. Chen, Unified implicit kinetic scheme for steady multiscale heat transfer based on the phonon Boltzmann transport equation, *Phys. Rev. E* 96 (2017), 063311.
- [36] A. Vega-Flick, R.A. Duncan, J.K. Eliason, J. Cuffe, J.A. Johnson, J.-P. Peraud, L. Zeng, Z. Lu, A.A. Maznev, E.N. Wang, Thermal transport in suspended silicon membranes measured by laser-induced transient gratings, *AIP Adv.* 6 (2016) 121903.
- [37] K.C. Collins, A.A. Maznev, Z. Tian, K. Esfarjani, K.A. Nelson, G. Chen, Non-diffusive relaxation of a transient thermal grating analyzed with the Boltzmann transport equation, *J. Appl. Phys.* 114 (2013) 104302.
- [38] H. Gao, L. Sun, J.-X. Wang, PhyGeoNet: physics-informed geometry-adaptive convolutional neural networks for solving parameterized steady-state PDEs on irregular domain, *J. Comput. Phys.* 428 (2021) 110079.
- [39] M. Hu, Z. Yang, Perspective on multi-scale simulation of thermal transport in solids and interfaces, *Phys. Chem. Chem. Phys.* 23 (2021) 1785–1801.